

Enantioselective Se lattices for stable chiroptoelectronic processing media

Received: 6 December 2024

Accepted: 9 April 2025

Published online: 03 May 2025

 Check for updatesJunyoung Kwon^{1,2}, Jae Bum Jeon¹, Min Gu Lee¹, Serin Jeong¹, Won Jin Choi³,
Kyung Min Kim¹ & Jihyeon Yeom¹✉

Chiroptoelectronic devices are crucial for applications in quantum computing, spin optical communications, and magnetic recording. However, the limited efficiency and low stability of conventional circularly polarized light (CPL)-sensing materials have restricted their broader use. Here, we introduce atomic chiral Se nanorod (NRs) films as broadband CPL detectors, leveraging the intrinsic chirality and stability of Se nanocrystals. We also perform incident circular polarization (ICP)-Raman optical activity (ROA) to explore the chiroptical activity of the large-area films. The Se NRs thin films detected CPL across a broad range from ultraviolet (UV) to short-wavelength infrared (SWIR), with a responsivity dissymmetry factor of up to 0.4, maintaining high stability under ambient conditions for longer than 13 months. CPL-sensitive Se NRs with intrinsic chirality have potential applications in chiral photonic synapses, chiral spin devices, and CPL-sensitive photocatalysts. ICP-ROA mapping also advances the analysis of 2D chiral materials.

Circularly polarized light (CPL) offers valuable functionalities in various optical devices, from quantum computing and spin optical communications to magnetic recording^{1–5}. The detection and manipulation of the spin angular momentum of light have become key technologies for exploiting this intriguing aspect of light. Chiral organic polymers⁶ and organic-inorganic hybrid materials (chiral perovskites)^{7–9} have emerged as promising candidates for CPL detection, allowing the integration or miniaturization of conventional CPL-sensitive photodetectors that typically require wave plates and polarizing filters. For example, Chen et al. reported a photodetector using a chiral hybrid perovskite which showed a responsivity dissymmetry factor (g_{res}) of 0.1 under 395 nm CPL laser irradiation¹⁰. Similarly, Peng et al. developed a VIS-NIR dual-modal CPL detector using chiral perovskite bulk crystals, achieving g_{res} values of up to 0.13 and 0.1 for 520 and 800 nm illumination, respectively¹¹. Despite these advances, CPL photodiodes based on organic polymers and hybrid perovskite materials suffer from long-term instability when exposed to humid environments, high temperatures, and ultraviolet (UV) light. The volatile and hygroscopic nature of the organic components also poses challenges for commercialization^{12–14}. Although all-inorganic achiral perovskites have

been introduced as more stable alternatives, the incorporation of organic cations in chiral perovskites synthesis remains necessary, as these cations are essential for imparting chirality to the system. Plasmonic metamaterials offer a stable option for detecting CPL; however, their heat generation leads to energy loss and potential device damage, while limited number of peaks and detection wavelength range also hinder further multiplexing and the use of wavelengths beyond the NIR^{2,15,16}. In contrast, short-wavelength infrared (SWIR) CPL photodetectors provide significant advantages, such as a broader detection range, improved imaging through various materials, reduced scattering for clearer images, enhanced night vision capabilities, and improved material identification^{17–19}. Therefore, it is imperative to develop broadband photodetectors based on all-inorganic materials that can effectively detect the spin angular momentum of light across a broad wavelength range, extending to SWIR, with long-term stability.

Chiral inorganic nanocrystals with non-centrosymmetric atomic structures are promising candidates for broadband CPL photodetectors. Crystals with atomic chiral lattice structures are more likely to exhibit broadband optical activity from visible to IR due to their

¹Department of Materials Science and Engineering, Korea Advanced Institute of Science and Technology (KAIST), Daejeon, Republic of Korea. ²Major of Nanotechnology Engineering, Pukyong National University, Busan, Republic of Korea. ³Physical and Life Sciences, Lawrence Livermore National Laboratory, Livermore, California, USA. ✉e-mail: jhyeon@kaist.ac.kr

intrinsic anisotropy in both inter- and intra-band transitions^{20–22}. A significant condition is that these crystals possess consistent handedness (left or right). For example, Se naturally has a non-centrosymmetric lattice structure of chiral space group, but its orientation (left or right) forms randomly. Therefore, the technology to induce or selectively form crystals in one direction is crucial for versatile applications.

It is also important to accurately analyze whether the lattice structure of the obtained crystal is left- or right-oriented. Atomic-resolution scanning transmission electron microscopy (STEM) imaging with tilting techniques was employed to precisely determine the atomic-level chirality^{23–25}. However, this technique is time-consuming and requires precise TEM with aberration correctors, making it unsuitable for the statistical analysis of nanocrystal handedness. Although Ben-Moshe et al. correlated the shape handedness with the crystal handedness of chiral Te nanocrystals and analyzed the occurrence of left-handed and right-handed crystals using the scanning electron microscopy (SEM) technique²⁶, this method is limited to nanocrystals with their overall shape or chiral morphology. Therefore, there is a need for facile and universal analytical techniques to determine the crystal handedness of nanocrystals.

In this study, we report the enantioselective synthesis of Se nanorods (NRs), which possess an intrinsic non-centrosymmetric trigonal atomic structure. Se materials also have stable photogalvanic properties, making them an ideal candidate for a broadband CPL detector^{10,11,27–30}. Utilizing these properties, we designed a CPL photodetector with a thin film of Se NRs on the top electrode, capable of detecting a broad range of CPL from UV to SWIR. We also performed a two-dimensional (2D) Raman optical activity (ROA) mapping to statistically determine the handedness of the crystal. This chiral 2D analysis revealed that Se NRs had left- ($P3_21$) or right-handed ($P3_121$) lattice structures when synthesized using *L*-cysteine (*L*-Cys) or *D*-cysteine (*D*-Cys) under certain conditions. The photodetector showed a high asymmetric responsivity for photons with different handedness, reaching values of up to 0.4, which is comparable to or even higher than the values reported for chiral perovskites^{10,27–33}. We believe that our Se NRs with intrinsic/atomic chirality, their thin films, and the 2D ROA mapping technique pave the way for chiroptical electronic devices and large-area chirality analysis tools.

Results and discussion

Structural analysis and growth mechanism

Trigonal Se can exhibit two different chiralities in its crystal structure, as shown in Fig. 1a: $P3_21$ for right-handed crystals and $P3_121$ for left-handed crystals. To synthesize trigonal Se nanocrystals with controlled crystal handedness, we adopted a screw dislocation-driven growth method for 1D nanostructures under low supersaturation conditions²⁶, utilizing chiral cysteine (Cys) ligands to bias the synthesis towards one-handedness. The synthesized Se nanocrystals are referred to as *L*- and *D*-Cys-Se NRs when *L*- and *D*-Cys are used as chiral ligands, respectively, and *DL*-Cys-Se NRs when an equivalent racemic mixture of *L*- and *D*-Cys is used. Transmission electron microscopy (TEM) and SEM analysis revealed that *L*- and *D*-Cys-Se NRs were approximately 105 ± 21 nm and 126 ± 27 nm in diameter, 1020 ± 290 nm and 977 ± 442 nm in length, respectively, whereas *DL*-Cys yielded larger Se NRs with diameters of 183 ± 53 nm and lengths of 1640 ± 790 nm (Fig. 1b and Supplementary Fig. 1). X-ray diffraction analysis confirmed that the Cys-Se NRs had a trigonal Se crystal structure, consistent with the ICDD PDF number 06-0363 (Fig. 1c and Supplementary Fig. 2).

TEM analysis revealed interesting contrasts and voids within the Se NRs (Fig. 1d–f). We noted that they originated from screw dislocations formed during chiral growth. Chiral molecules play a crucial role in this process and are highly sensitive to the pH of the growth solutions. A low reduction rate leads to low monomer supersaturation, which in turn promotes screw dislocation-mediated growth. The

moderately low pH of the reaction solution can therefore bias chiral crystal growth in the presence of chiral molecules^{26,34–36}. The correlation between pH, morphology, and optical activity is supported by the flat circular dichroism (CD) spectra observed at pH > 10 (Supplementary Fig. 3).

However, our *L*-Cys-Se and *D*-Cys-Se NRs did not exhibit significant morphological differences in the SEM and TEM images, suggesting a lack of correlation between shape and atomic chirality, unlike the previously reported method²⁶. Therefore, we analyzed the atomic chirality of a single nanorod using a high-resolution STEM tilting method (Fig. 1g–i). High-angle annular dark-field (HAADF)-STEM images of *L*-Cys-Se NR from the [120] and [010] zone axes after tilting 30° to the right (counterclockwise) around the *c*-axis from the [120] zone axis closely matched the simulated atomic arrangement of a left-handed $P3_21$ Se crystal. This indicates the potential for determining the crystal handedness of Se nanocrystals using an atomic-resolution STEM tilting series.

ICP-ROA spectral analysis

While high-resolution STEM-based analysis provides accuracy and allows for individual analysis, it also has significant limitations, including the requirement of expensive instruments and expert measurement skills. To address these limitations, we applied ICP-ROA to assess the intrinsic chirality of chiral Se NRs. This is because, unlike CD spectroscopy, which probes electronic transitions in the visible and near-infrared regions, ICP-ROA detects chiral phonons, enabling the characterization of chirality within inorganic crystal lattices by revealing long-range coherent vibrations and chiral distortions at the atomic level^{37,38}. Thus, we collected the Raman shift signals from a broad area with a diameter of ~ 15 μ m, allowing the averaged Raman shift signals from multiple Se NRs to be reflected in the spectra. From the Raman spectra of the Se NRs shown in Fig. 2a, the 1st order Raman shift peaks at 102, 143, 233, and 237 cm^{-1} can be assigned to the rotation about the chain *z*-axis, rotation about the *x*- or *y*-axis of the chain, asymmetric breathing, and symmetric breathing phonon modes of the lattice structures, respectively. The peaks at 437 and 459 cm^{-1} can be attributed to the 2nd-order spectra of trigonal Se³⁹.

ICP-ROA ($I_{\text{RCP}} - I_{\text{LCP}}$) spectra using CPL excitation, depicted in Fig. 2b, c shows positive and negative signs for *L*- and *D*-Cys-Se NRs, indicating left-handed (M) and right-handed (P) helix crystal structures, respectively⁴⁰. The sign of the ICP-ROA peak from the quartz substrate remained consistent throughout the measurements of different samples, serving as a reference (Supplementary Fig. 4). Furthermore, when defining the ROA dissymmetry (circular intensity difference, CID, Δ) values as $(I_{\text{RCP}} - I_{\text{LCP}})/(I_{\text{RCP}} + I_{\text{LCP}})$ where I_{RCP} and I_{LCP} represent the Raman intensities of RCP and LCP light, respectively, the Δ -values for *L*-Cys-Se and for *D*-Cys-Se were approximately 0.1 and -0.1 , respectively (Fig. 2d). These values are significantly higher than those typically observed in optically active molecules, which have Δ -values up to 10^{-3} ^{41,42}. This strong ROA dissymmetry can be attributed to the high occurrence of one-handedness in the intrinsic chirality of the inorganic crystals (either $P3_21$ or $P3_121$).

To utilize ICP-ROA techniques for investigating the enantiomeric excess ratio of Se NRs, we adopted a 2D microscale mapping method of ICP-ROA, which is useful for statistical analysis to determine the handedness of intrinsically chiral nanocrystals across a desired area (Fig. 2e). To obtain non-overlapping ICP-ROA signals from Se NRs, we deposited Se NRs at an air-water interface in a thin film form, inspired by a previous report (Supplementary Fig. 5)⁴³.

ICP-ROA mapping for 2D chiral analysis

Raman signals were collected from 100 points over a 50×50 μ m area on the *L*-, *D*-, and *DL*-Cys-Se NRs films (Fig. 2f–h). The main 1st order Raman shift peak at 237 cm^{-1} was selected to plot 2D mapping. The results showed that *L*-Cys-Se NRs showed approximately 50%

enantiomeric excess (ee), while *D*-Cys-Se NRs exhibited -44% ee. (Fig. 2i, j, and Supplementary Fig. 6). In contrast, *DL*-Cys-Se indicates a minimal enantiomeric excess. In the case of *DL*-Cys-Se NRs, the occurrence ratios were 49% for a positive sign and 51% for a negative sign, displaying a minimal value of -1% ee, which indicates an almost racemic occurrence of *M*- and *P*-helix nanocrystal structures in the presence of racemic Cys (Fig. 2k and Supplementary Fig. 7). These results demonstrate that 2D ICP-ROA mapping techniques can effectively monitor the population ratios of chiral nanocrystals and determine the handedness of chiral NRs using spatial distribution information.

Chiroptical activity originates from the intrinsic chiral structures

Chiral crystals possess chiral charge density waves that result in chiral electronic band structures⁴⁴. Thus, materials with chiral atomic arrangements can exhibit optical activity where electron transitions occur, unlike materials with mere morphological chirality. Se NRs are expected to exhibit broadband optical activity from visible to the IR range in both inter- and intra-band

transitions due to their intrinsic atomic chirality. Consequently, chiroptical analysis was conducted over a broad wavelength range from UV to 2500 nm. The thin film deposition of Se NRs facilitated broadband optical analyses. *L*-, *D*-, and *DL*-Cys-Se NRs exhibited a broad extinction peak from 180 to 2500 nm (Fig. 3a, b). *L*- and *D*-Cys-Se NRs presented broad optical activity from 180 to 2500 nm, with the CD spectra being mirror images of each other, whereas *DL*-Cys-Se NRs showed no optical activity (Fig. 3c). Notably, the random orientation of the Se NRs enabled us to rule out linear birefringence and linear dichroism effects in the CD signals (Supplementary Fig. 8). In addition, Se NRs dispersed in ethanol showed the same CD signal trend as the CD film (Supplementary Fig. 9). The CD peaks from the UV to the visible range can be ascribed to quantum confinement and the intrinsic bandgap (-1.8 eV), whereas those at 480 and 650 nm can be assigned to interband transitions from covalent bonds within the Se chain and weak interchain van der Waals interactions⁴⁵. The CD peaks between 800 and 2500 nm can be attributed to the electron transition to defect states within the bandgap, possibly caused by screw dislocations⁴⁶⁻⁴⁹. Furthermore, the chiroptical

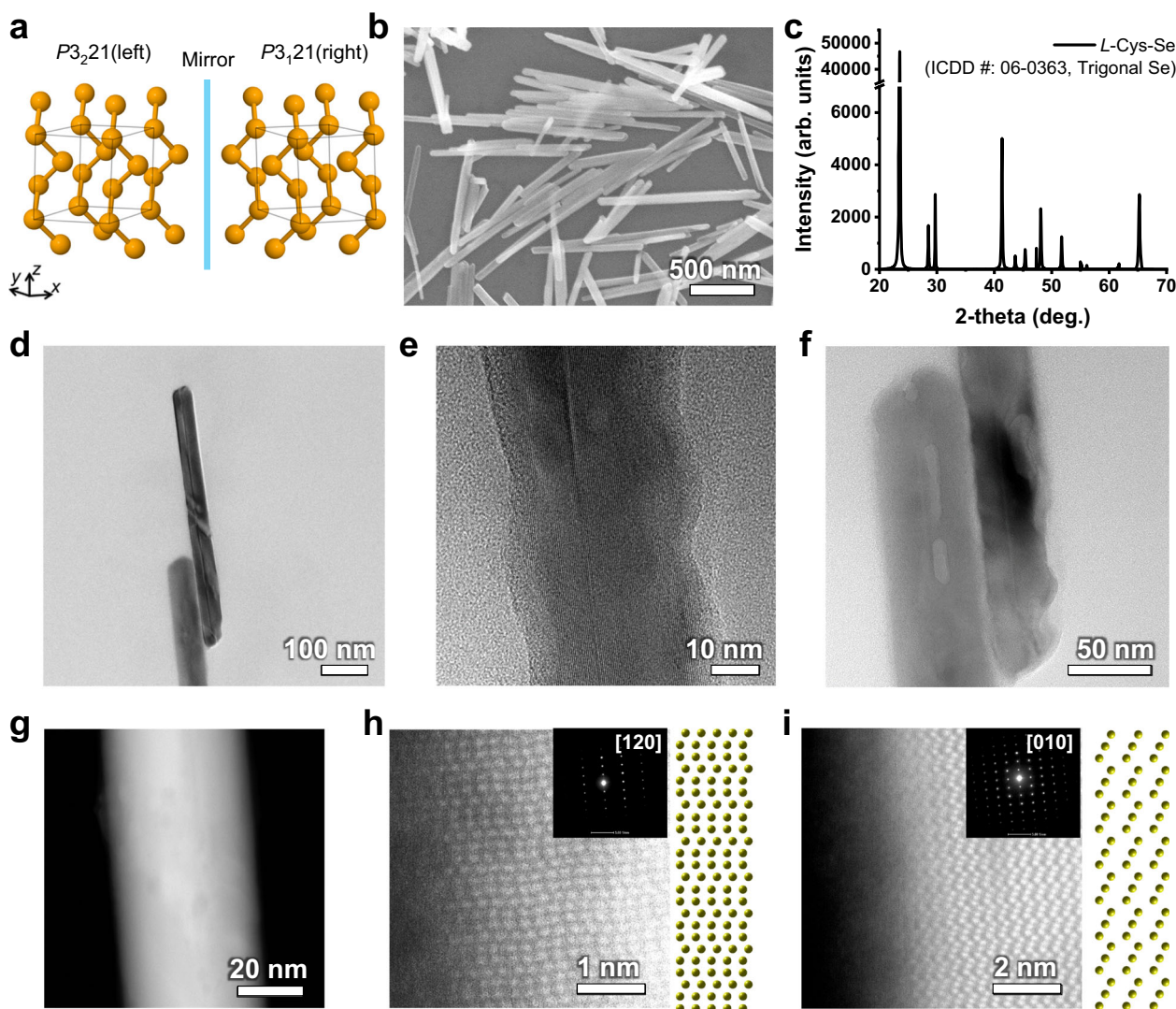
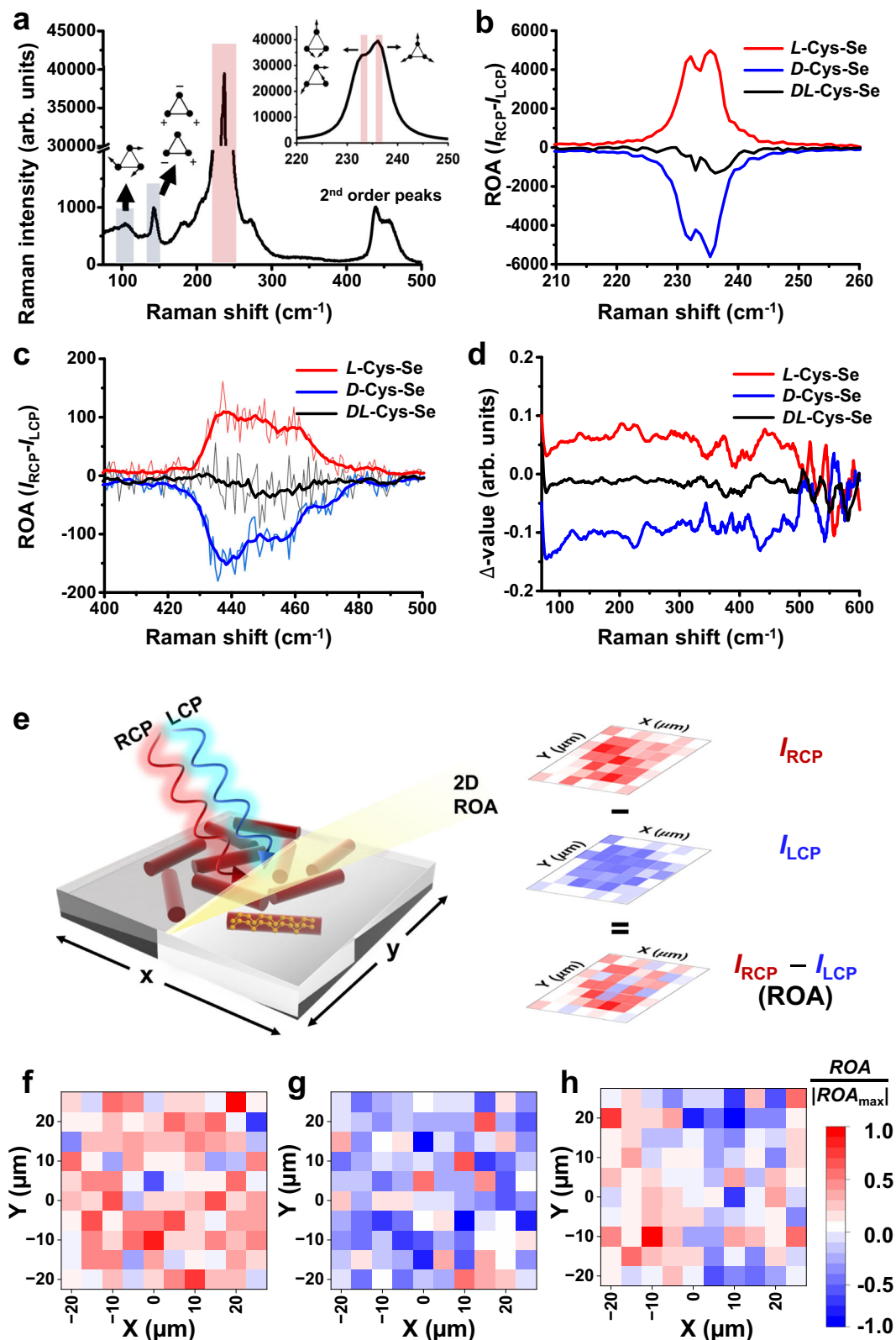


Fig. 1 | Morphology and atomic structure analysis of cysteine (Cys)-Se NRs. **a** Schematic of the atomic structure of left-handed (LH) $P3_21$ and right-handed (RH) $P3_121$ Se crystals. **b** Scanning electron microscopy (SEM) image and **c** X-ray diffraction (XRD) pattern, **d–f** transmission electron microscopy (TEM) images of *L*-Cys-Se NRs showing screw dislocation-induced **e** contrast and **f** voids, **g** high-angle

annular dark-field (HAADF)-scanning transmission electron microscopy (STEM) image, **h, i** (left images) high-resolution HAADF-STEM image of **h** the $[120]$ zone axis, **i** the $[010]$ zone axis tilted 30° to the right from the $[120]$ zone axis of *L*-Cys-Se. Insets show selected area diffraction (SAD) of *L*-Cys-Se (right pattern) and simulated atomic arrangement of the $P3_21$ Se crystal.



activity was significant throughout the UV to SWIR region, with dissymmetry of absorption (g_{CD}) values up to 0.008, due to the high enantiomeric excess of the intrinsically chiral Se NRs (Fig. 3d), where the g_{CD} was calculated using the equation: $g_{CD} = CD / (32980 \times \text{absorbance})$. Comprehensive Mueller polarimetry analysis was also used to assess the intrinsic chiral responses of the CD and circular birefringence, excluding

possible artifacts, such as linear dichroism and linear birefringence of the film (Supplementary Fig. 10)³³.

Trigonal Se is generally recognized as a p-type semiconductor with photocurrent property, where photon absorption increases hole density, thereby enhancing conduction⁵⁰⁻⁵². The presence of screw dislocations introduces defect states that trap electrons, allowing charge carriers (holes) to be generated with energy lower than the

Fig. 2 | Raman optical activity (ROA) and 2D ROA mapping of Cys-Se nanorod (NR) film. **a** Raman spectra of *L*-Cys-Se NR film and the type of phononic oscillation of atoms. The gray shaded area indicates the first-order Raman peaks at 102 and 143 cm^{-1} , which are attributed to rotational modes about the chain *z*-axis and the *x*- or *y*-axis, respectively. The pink shaded area highlights the Raman peaks at 233 and 237 cm^{-1} , corresponding to the asymmetric and symmetric breathing phonon modes of the lattice structure. The inset shows an enlarged view of the Raman peak region (pink shaded area). **b**, **c** incident circular polarization (ICP)-ROA spectra of

b first-order, **c** second-order Raman shift, **d** Δ -value spectra of *levo* (*L*-), *dextro* (*D*-), racemic (*DL*-) Cys-Se NR films. The Δ -value, or circular intensity difference (CID), is defined as $(I_{\text{RCP}} - I_{\text{LCP}})/(I_{\text{RCP}} + I_{\text{LCP}})$ where I_{RCP} and I_{LCP} represent the Raman intensities of right- and left-circularly polarized (RCP and LCP) light, respectively. The raw data are shown as shaded curves, and the smoothed spectra are overlaid as solid lines. **e** Schematic illustration of the 2D ROA mapping analysis and data analysis. **f–h** 2D mapping of the normalized ICP-ROA of **f** *L*-, **g** *D*-, **h** *DL*-Cys-Se NRs at the Raman shift peak of 237 cm^{-1} .

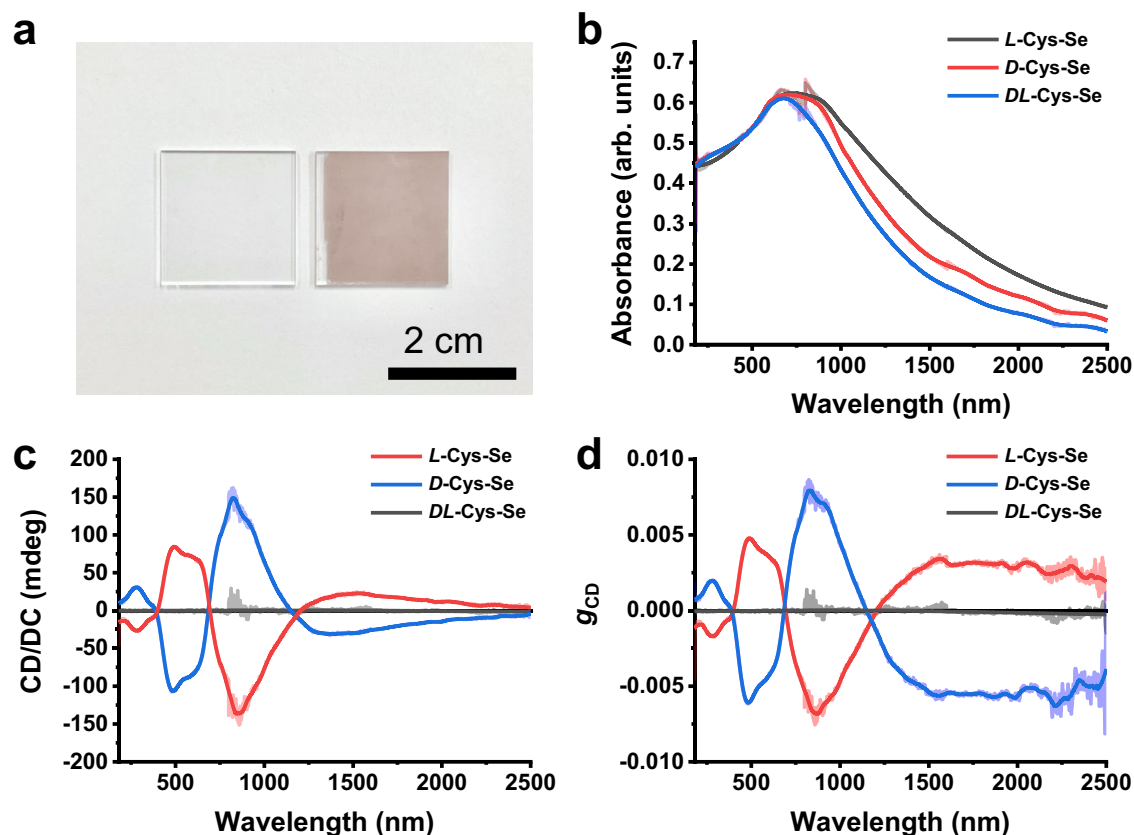


Fig. 3 | Intrinsic chiral Cys-Se NRs with broadband chiroptical activity from ultraviolet (UV) to short-wave infrared (SWIR). **a** Digital image of a thin film of *L*-Cys-Se NRs on a quartz substrate used for optical measurement. **b** Extinction

spectra, **c** smoothed circular dichroism (CD) spectra, **d** dissymmetry factor of absorption (g_{CD}) spectra of chiral Cys-Se NR films. The shaded curves in (**b–d**) represent the raw data, while the solid lines indicate the smoothed spectra.

bandgap (800 nm–2500 nm). Furthermore, the trigonal Se NRs can be deposited into a two-dimensional thin film by using interfacial assembly technique on water surface⁴³. This method, combined with our findings on broadband chiroptical activity, inspired us to apply these materials in a broadband CPL photodetector. To achieve this, we fabricated a photodetector device with a thin film of randomly distributed Se NRs (~30 nm thick) deposited on an interdigitated Au electrode with a thickness of 50 nm, as shown in Fig. 4a, b. When exposed to 488 nm wavelength light, the Cys-Se NR photodetectors generated a stable current with minimal variation within 1 nA across different devices. (Supplementary Fig. 11). Furthermore, Se NR photodetector exhibited fast response and reset time within 1 s with the current rising and decay process with a reset time of less than 0.2 s (Supplementary Fig. 12)^{53–55}. The slope of the *I*-*V* curve changed depending on whether the photodetector was illuminated with left-circularly polarized (LCP) light, right-circularly polarized (RCP) light, and linearly polarized (LP) light (Fig. 4c and Supplementary Fig. 13). Since *L*-Cys-Se NRs absorbed LCP light more effectively than RCP light at 488 nm, the CPL detector exhibited a steeper slope for LCP incident light in the *I*-*V* curve compared to RCP and LP light. This trend was

consistently observed across different illumination times and temporal photoresponses (Fig. 4d, e). Notably, the CPL photodetector did not generate a photocurrent in the absence of light, confirming the presence of an evident photocurrent in the Se NR film. It can be noted that the charges between adjacent rods can be transported through hopping mechanism where charge carriers in nanorods film hop from one rod to another. A network of interconnected nanoparticles also provides continuous pathways for charge carriers to move towards the electrodes via percolation pathways making the device work^{56,57}. The retarder angle-dependent photocurrent result indicates that the photocurrent exhibits a sinusoidal pattern as the ellipticity of the incident light is varied, with the highest photocurrent values observed at -45° and 135° , highlighting the dependence of photocurrent on the degree of light ellipticity (Fig. 4f). Thus, the *L*-Cys-Se NRs have higher photocurrent properties under left-handed elliptical light than under right-handed elliptical light at 488 nm, consistent with the CD spectra. Meanwhile, the light intensity-dependent photocurrent results also showed a consistent photoresponsivity of ca. 20 mA/W over a range of light intensities from 2 to 10 mW/cm^2 (Fig. 4g). The photoresponsivities of *L*- and *D*-Cys-Se photodetectors were measured

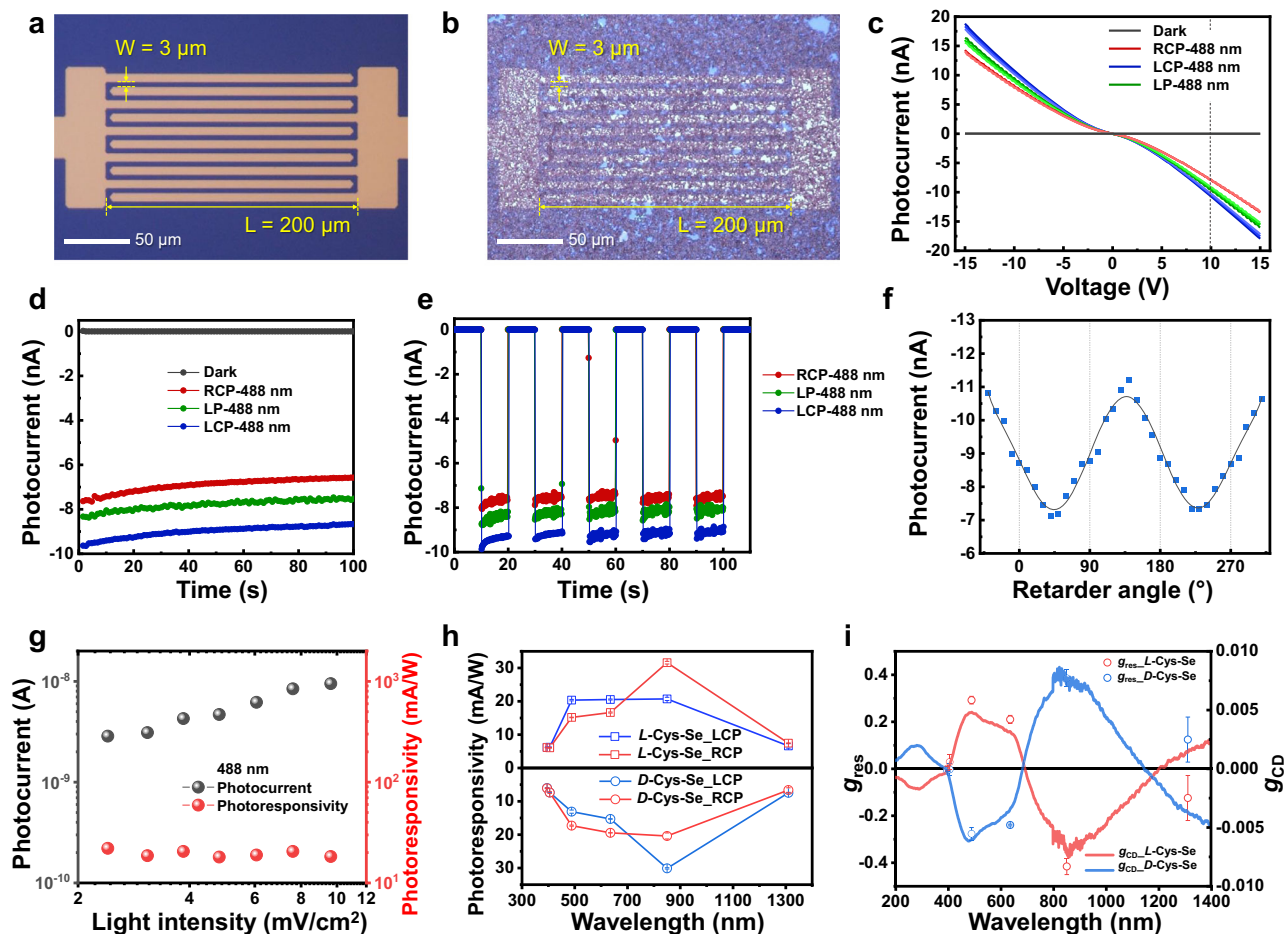


Fig. 4 | Se NR film as a broadband circularly polarized light (CPL) photodetector. **a, b** Microscopic images of **a** Au (50 nm)/Cr (3 nm)/SiO₂ (300 nm)/Si substrates, **b** *L*-, *D*-, or *DL*-Cys-Se/Au/Cr/SiO₂/Si substrates. **c** *I*-*V* curves of *L*-Cys-Se device under dark conditions, LCP 488 nm, RCP 488 nm, and LP 488 nm light illumination. The dotted line indicates the current when applying 10 V voltage, which is chosen for irradiation time-dependent photocurrent in the following figures (**d**–**i**) with 488 nm laser to avoid potential device degradation while maintaining a high photocurrent signal⁵⁰, where the light intensity was 9 mW cm⁻² after the light passed a linear polariser and a quarter-wave plate (retarder). **d** Photocurrent of *L*-Cys-Se device under dark, LCP 488 nm, RCP 488 nm, LP 488 nm irradiation as a function of illumination time. **e** Photoresponse of *L*-Cys-Se

films under LCP and RCP 488 nm light, with 10-s on/off intervals. **f** Photocurrent as a function of light ellipticity, defined by the angle between the linear polarizer and the quarter-wave retarder. The data points represent the measured photocurrent values, and the solid line is a polynomial fit to the data. **g** Light intensity-dependent photocurrent and photoresponsivity at 10 V under 488 nm incident unpolarized light. **h** Wavelength-dependent photoresponsivity, **i** Calculated wavelength-dependent responsivity dissymmetry factor (g_{res}) values of *L*-, *D*-Cys-Se CPL photodetector under LCP and RCP light illumination at 395, 405, 488, 635, 850, and 1310 nm, alongside the g_{CD} spectra for comparison. The data points represent the average g_{res} values, and the solid lines correspond to the g_{CD} spectra. Error bars in (**h**) and (**i**) indicate the standard deviation.

at 405, 488, 635, 850, and 1310 nm under RCP and LCP light illumination. As shown in Fig. 4h, the photoresponsivity of *L*- and *D*-Cys-Se photodetectors varies with wavelength and handedness of light, ranging between of 5 and 30 mA/W which are typical values for trigonal Se-based photodetectors^{58–60} and sufficient for general photodetection^{61,62}. *L*- and *D*-Cys-Se photodetectors exhibited opposite trends in photoresponsivity, with the trend at 488 and 635 nm being reversed at 850 and 1310 nm. Note that the photocurrent beyond 1400 nm was negligible due to the limited density of intermediate states^{49,63,64}. The distinguishability of different photoresponsivities to LCP and RCP can be quantified using an anisotropy factor ($g_{res} = 2(R_L - R_R)/(R_L + R_R)$) where R_L and R_R are photoresponsivity under LCP and RCP, respectively. Figure 4i shows that the g_{res} values at 395, 488, 635, 850, and 1310 nm followed a similar trend to the g_{CD} spectra, indicating the highest g_{res} value up to -0.4 at 850 nm, due to the high g_{CD} of *L*- and *D*-Cys-Se NRs with a high enantiomeric excess ratio. The lower g_{CD} values of the Se photodetectors compared to the g_{res} values can be attributed to the non-specific extinction from the scattering component in the CD spectra, which does not affect the g_{res} values. The Se

NR films presented in this work demonstrate broader chiroptical activity in both g_{res} and g_{CD} , spanning from the UV to the SWIR region, while maintaining comparable or even higher values than previously reported structural, organic, and hybrid CPL detectors, which are typically limited to narrower ranges within the visible to near-infrared region^{6,65–67}. Thus, chiral Se NRs can serve as broadband CPL photodetectors with high distinguishability. In addition, the Se NRs are stable under ambient conditions, making photodetectors made from these materials nearly semi-permanent.

Given that stability is a crucial specification for devices, the long-term stability of the Se NR CPL detector was examined after aging for 13 months under ambient laboratory conditions (Fig. 5). The g_{CD} and extinction spectra of both freshly prepared and 13-month-old films exhibited negligible differences in both sign and peak positions across UV to SWIR region (Fig. 5a–c). In addition, no significant degradation in photocurrent performance was detected between the 13-month-old film and the fresh film, indicating consistent current generation trends when illuminated with RCP, LP, and LCP lights (Fig. 5d). Figure 5e shows the nonlinear trend in the photocurrent over long-term aging,

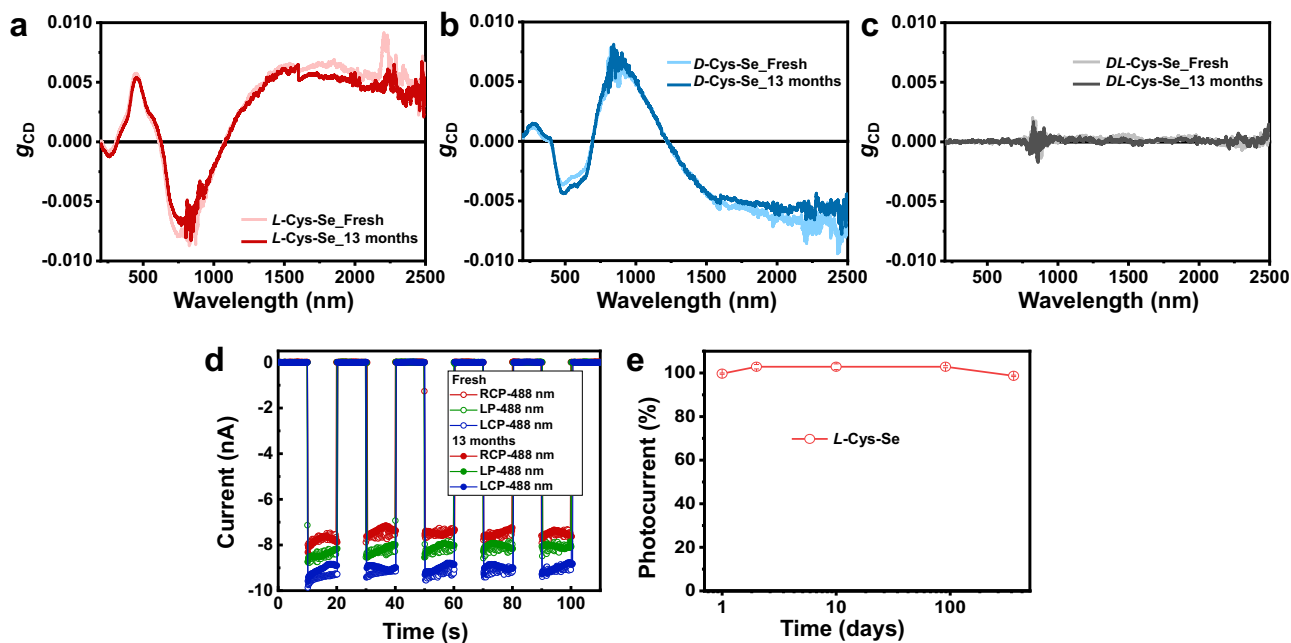


Fig. 5 | Long-term stability of Se NR film in ambient conditions. g_{CD} spectra of fresh and 13-month-old **a** *L*-, **b** *D*-, and **c** *DL*-Cys-Se NR films. **d** Photoresponse of fresh and 13-month-old *L*-Cys-Se films under 488 nm LCP, LP, and RCP light, with

10-s on/off intervals at an applied voltage of 10 V. **e** Relative photocurrent of *L*-Cys-Se films at different time points compared with the fresh film. Error bars indicate standard deviation.

where the initial increased photocurrent can be attributed to the interfacial and lattice relaxation effect upon aging^{68–71}.

In conclusion, we report an enantioselective synthetic method for producing chiral Se NRs with controlled atomic crystal chirality. Although the overall morphology of the synthesized Se NRs was identical to that of symmetric NRs, the atomic chirality was successfully resolved using the 2D ICP-ROA mapping technique. The 2D ROA mapping provides a universal tool to statistically probe enantioexcessive ratio of chiral materials with the intrinsic crystal chirality. The atomically chiral Se NRs showed strong chiroptical activity across a broad wavelength range from UV (180 nm) to SWIR (2500 nm). The CPL photodetector fabricated using these Se NRs showed effective CPL photoresponsivity at the selected wavelengths ranging from 395 nm to 1310 nm, with g_{res} values of up to 0.4. Furthermore, the photodetector remained highly stable for over 13 months under ambient conditions, attributed to the inorganic nature of the materials. The broadband CPL detectors with the atomically chiral Se NRs that can detect light from UV to SWIR can open up applications in security, quantum information and communication, and the biomedical field, compared to traditional CPL detectors that only detect a limited light range. For example, these CPL detectors enhance security by detecting and countering stealth technologies designed to evade detection in the UV-Vis range, as well as enabling polarization-based encryption and decryption methods over a wide spectral range. In medical applications, these detectors could be employed in multispectral imaging systems to detect and differentiate between various tissues and biological structures, enhancing the ability to diagnose and monitor conditions that exhibit chiral signatures in deeper tissues. This system can also be applied in various fields that require intrinsic chirality of materials, such as low-power spintronics, quantum information, and photo-catalysis, leveraging the additional degree of freedom provided by light chirality.

Methods

Materials

Selenium dioxide (SeO_2 , $\geq 99.9\%$), *L*-cysteine (*L*-Cys, 98%), *D*-cysteine (*D*-Cys, 99%), sodium hydroxide (NaOH, 95%), ethanol (99%), and

hydrochloric acid (37%) were purchased from Sigma-Aldrich and used without further purification. All water used was ultrapure from a Millipore system (18.2 M Ω -cm).

Preparation of atomically chiral Se NRs

Atomically chiral selenium NRs were synthesized via a chemical reduction method in a 40 °C water bath. First, 0.5 mL of SeO_2 solution (0.1 M) was added to 4.5 mL of Milli-Q water. The reaction solution was then mixed with 1 mL Cys solution (0.1 M) (*L*-Cys, *D*-Cys, *DL*-Cys for *L*-Cys-Se, *D*-Cys-Se, *DL*-Cys-Se) and 0.5 mL of SDS solution (0.1 M). The pH of the mixture was adjusted to 8. Finally, 7 mL ethanol was added to the mixture. The solution was stirred at 300 rpm for 3 h at 40 °C, where the g_{CD} value at the peak wavelength was maximized (Supplementary Fig. 14). During the reaction, the color of the solution changed from orange to brick red, indicating a transition from amorphous to trigonal Se NRs. The final products were washed and collected by centrifugation with ethanol and water after adjusting the pH of the solution to 11 to remove cysteine crystals. The Se NRs were then redispersed in ethanol for further characterization (Supplementary Figs. 15, 16). It is noteworthy that the synthesis of Cys-Se NRs can be carried out at room temperature using elemental selenium as a precursor, with water and ethanol as co-solvents. This process is environmentally benign, as it does not produce harmful fumes, allowing it to be conducted under ambient conditions on a standard laboratory bench with basic equipment. Furthermore, the synthesis is streamlined, as it does not require separate steps for nucleation and growth. The nucleation of amorphous Se is initiated immediately upon the addition of Cys to the mixture, followed by spontaneous growth into trigonal Se during the reaction with ethanol.

Preparation of a thin film of chiral Se NRs

A chiral Se nanorod thin film was prepared following a previously reported method⁴³. Briefly, atomic chiral Se NRs were dispersed in 1-butanol by sonication at a concentration of 1 mg/mL. The Se nanorod dispersion was then dropped onto the water surface to form a thin film at the air-water interface. The film was subsequently transferred onto a quartz wafer (20 × 20 mm).

Raman analysis

ICP-ROA spectra were obtained using a LabRAM HR Evolution spectrometer (Horiba Co., Japan). A laser beam with a wavelength of 785 nm was focused on a spot approximately 15 μm in diameter on the Cys-Se NR film surface using a 10 \times objective lens to acquire ROA spectra, as it provides an averaged signal over multiple nanorods. The incident RCP and LCP light were generated by passing linearly polarized light through a quarter-wave plate. For 2D ROA mapping, a 100 \times objective lens with a 600 grating/mm was used, resulting in a spot size of 1.5 μm , where the minimized spot size enabled statistical analysis at the level of individual nanorods. In addition, light power of 161.6 μW and 62.5 μW were used for *L*-, *D*-Cys-Se and *DL*-Cys-Se, respectively, by changing neutral density filters. The spectral window ranged from 50 to 500 cm^{-1} . The mapping was performed over a 10 \times 10 grid by scanning from $-20 \mu\text{m}$ to 25 μm with an acquisition time of 10 s. The enantiomeric excess (ee%) was calculated using the formula $100 \times (A - B)/(A + B)$, where *A* and *B* are the number of positive and negative ROA values, respectively.

Electron microscopy and optical characterization

Bright-field HR-TEM images were obtained using a Libra 200 MC TEM (Carl Zeiss, Germany) equipped with a ZrO/W-field emitter system (Schottky emitter), a monochromator (CEOS, Germany), an Imaging Cs-Corrector (CEOS, Germany), and a Corrected OMEGA in-column energy filter, operated at 200 kV at the Korea Basic Science Institute (KBSI) on the Daejeon Campus, South Korea. HAADF-STEM images were obtained at 200 kV using a scanning transmission electron microscope (Titan cubed G2 60-300; FEI) with double Cs correctors at the KAIST Analysis Center for Research Advancement (KARA). Samples for XRD and Raman spectral analyses were prepared by drop-casting the powder onto Si substrates. Absorption and CD spectra were recorded using a CD spectrometer (J-1700, JASCO, Japan).

CPL photodetector fabrication and photocurrent measurement

Top Au gate electrodes (50 nm) were deposited via e-beam evaporation and patterned using shadow masks. The active area of the device had a channel length (*L*) of 200 μm and a gap width (*W*) of 3 μm , respectively. The *L*- or *D*-Cys-Se NR films were deposited onto the interdigitated Au electrodes by transferring the *L*- or *D*-Cys-Se NRs thin films onto water-air surfaces. The electrical properties of the devices were evaluated using a Keithley 4200A-SCS instrument. The photoresponsivity of the photodetector under light illumination was calculated using the following equation based on the previous report⁷²:

$$\text{Photoresponsivity} = (I_{\text{light}} - I_{\text{dark}}) / A_{\text{pt}} / (P / A_{\text{pd}}) \quad (1)$$

where I_{light} is the current measured under visible light illumination, while I_{dark} represents the dark current. The power of the incident light is denoted as *P*. The parameter A_{pt} corresponds to the effective device area, determined by the product of the channel width and thickness. Meanwhile, A_{pd} refers to the laser source's spot size. Although the channel area between the gold electrodes was not fully covered by Se NRs, which negatively affected the device's photoresponsivity values, we assumed the channel area was fully covered to simplify the calculation of the photodetection value.

Data availability

The Source Data underlying the figures of this study are available with the paper. All raw data generated during the current study are available from the corresponding authors upon request. Source data are provided with this paper.

References

1. Yang, S.-H., Naaman, R., Paltiel, Y. & Parkin, S. S. Chiral spintronics. *Nat. Rev. Phys.* **3**, 328–343 (2021).

2. Namgung, S. D. et al. Circularly polarized light-sensitive, hot electron transistor with chiral plasmonic nanoparticles. *Nat. Commun.* **13**, 5081 (2022).
3. Kwon, J. et al. Recent advances in chiral nanomaterials with unique electric and magnetic properties. *Nano Converg.* **9**, 32 (2022).
4. Kwon, J. et al. Chiroferromagnetic Quantum Dots for Chiroptical Synapse (ChiropS). *Adv. Mater.* <https://doi.org/10.1002/adma.202415366> (2025).
5. Jung, W. et al. Universal Chiral Nanopaint for Metal Oxide Biomaterials *ACS Nano* **19**, 8632–8645 (2025).
6. Song, I. et al. Helical polymers for dissymmetric circularly polarized light imaging. *Nature* **617**, 92–99 (2023).
7. Fan, C. C. et al. Chiral Rashba ferroelectrics for circularly polarized light detection. *Adv. Mater.* **34**, e2204119 (2022).
8. Li, X. et al. Robust spin-dependent anisotropy of circularly polarized light detection from achiral layered hybrid perovskite ferroelectric crystals. *J. Am. Chem. Soc.* **144**, 14031–14036 (2022).
9. Hu, R., Lu, X., Hao, X. & Qin, W. Organic chiroptical detector favoring circularly polarized light detecting from near-infrared to ultraviolet and magnetic field amplifying dissymmetry in detectivity. *Adv. Mater.* **35**, e2211935 (2023).
10. Chen, C. et al. Circularly polarized light detection using chiral hybrid perovskite. *Nat. Commun.* **10**, 1–7 (2019).
11. Peng, Y. et al. Realization of vis–NIR dual-modal circularly polarized light detection in chiral perovskite bulk crystals. *J. Am. Chem. Soc.* **143**, 14077–14082 (2021).
12. Zhao, X. et al. Accelerated aging of all-inorganic, interface-stabilized perovskite solar cells. *Science* **377**, 307–310 (2022).
13. Zhong, H. et al. All-inorganic perovskite solar cells with tetrabutylammonium acetate as the buffer layer between the SnO_2 electron transport film and CsPbI_3 . *ACS Appl. Mater. Interfaces* **14**, 5183–5193 (2022).
14. Akman, E. et al. The role of B-site doping in all-inorganic $\text{CsPbI}_x\text{Br}_{3-x}$ absorbers on the performance and stability of perovskite photovoltaics. *Energy Environ. Sci.* **16**, 372–403 (2023).
15. Li, W. et al. Circularly polarized light detection with hot electrons in chiral plasmonic metamaterials. *Nat. Commun.* **6**, 8379 (2015).
16. Basiri, A. et al. Nature-inspired chiral metasurfaces for circular polarization detection and full-Stokes polarimetric measurements. *Light Sci. Appl.* **8**, 78 (2019).
17. Mu, G. et al. Visible to mid-wave infrared PbS/HgTe colloidal quantum dot imagers. *Nat. Photonics* **18**, 1147–1154 (2024).
18. Yu, X.-Q., Sun, C., Liu, B.-W., Wang, M.-S. & Guo, G.-C. Directed self-assembly of viologen-based 2D semiconductors with intrinsic UV–SWIR photoresponse after photo/thermo activation. *Nat. Commun.* **11**, 1179 (2020).
19. Park, K.H. et al. Broad Chiroptical Activity from Ultraviolet to Short-Wave Infrared by Chirality Transfer from Molecular to Micrometer Scale. *ACS Nano* **15**, 15229–15237 (2021).
20. Ben-Moshe, A. et al. Enantioselective control of lattice and shape chirality in inorganic nanostructures using chiral biomolecules. *Nat. Commun.* **5**, 4302 (2014).
21. Jähnigen, S. Vibrational circular dichroism spectroscopy of chiral molecular crystals: insights from theory. *Angew. Chem. Int. Ed. Engl.* **62**, e202303595 (2023).
22. Jähnigen, S., Le Barbu-Debus, K., Guillot, R., Vuilleumier, R. & Zehacker, A. How crystal symmetry dictates non-local vibrational circular dichroism in the solid state. *Angew. Chem. Int. Ed. Engl.* **62**, e202215599 (2023).
23. Ma, Y., Oleynikov, P. & Terasaki, O. Electron crystallography for determining the handedness of a chiral zeolite nanocrystal. *Nat. Mater.* **16**, 755–759 (2017).
24. Dong, Z. & Ma, Y. Atomic-level handedness determination of chiral crystals using aberration-corrected scanning transmission electron microscopy. *Nat. Commun.* **11**, 1–6 (2020).

25. Calavalle, F. et al. Gate-tuneable and chirality-dependent charge-to-spin conversion in tellurium nanowires. *Nat. Mater.* **21**, 526–532 (2022).
26. Ben-Moshe, A. et al. The chain of chirality transfer in tellurium nanocrystals. *Science* **372**, 729–733 (2021).
27. Li, D. et al. Chiral lead-free hybrid perovskites for self-powered circularly polarized light detection. *Angew. Chem. Int. Ed. Engl.* **133**, 8496–8499 (2021).
28. Zhao, Y. et al. Chiral 2D-perovskite nanowires for Stokes photo-detectors. *J. Am. Chem. Soc.* **143**, 8437–8445 (2021).
29. Kwon, J. et al. Chiral Se Nanobrooms with Wavelength and Polarization Sensitive Scattering. *Adv. Funct. Mater.* **33**, 2300927 (2023).
30. Kim, M. et al. Bespoke selenium nanowires with comprehensive piezo-phototronic effects as viable p-type semiconductor-based piezo-photocatalysts. *Nano Energy* **114**, 108680 (2023).
31. Wang, J. et al. Spin-dependent photovoltaic and photogalvanic responses of optoelectronic devices based on chiral two-dimensional hybrid organic–inorganic perovskites. *ACS Nano* **15**, 588–595 (2020).
32. Liu, T. et al. High responsivity circular polarized light detectors based on quasi two-dimensional chiral perovskite films. *ACS Nano* **16**, 2682–2689 (2022).
33. Zhang, X. et al. Direct detection of near-infrared circularly polarized light via precisely designed chiral perovskite heterostructures. *ACS Appl. Mater. Interfaces* **14**, 36781–36788 (2022).
34. Zhu, J. et al. Formation of chiral branched nanowires by the Eshelby Twist. *Nat. Nanotechnol.* **3**, 477–481 (2008).
35. Meng, F., Morin, S. A., Forticaux, A. & Jin, S. Screw dislocation driven growth of nanomaterials. *Acc. Chem. Res.* **46**, 1616–1626 (2013).
36. Liu, Y. et al. Helical van der Waals crystals with discretized Eshelby twist. *Nature* **570**, 358–362 (2019).
37. Er, E., Chow, T. H., Liz-Marzán, L. M. & Kotov, N. A. Circular polarization-resolved Raman optical activity: a perspective on chiral spectroscopies of vibrational states. *ACS Nano* **18**, 12589–12597 (2024).
38. Kwon, J. et al. Chiral Spectroscopy of Nanostructures. *Acc. Chem. Res.* **56**, 1359–1372 (2023).
39. Cooper, W. C. The physics of selenium and tellurium. In *Proc. International Symposium Held at Montreal* (Elsevier, 2013).
40. Palomo, L. et al. Raman optical activity (ROA) as a new tool to elucidate the helical structure of poly (phenylacetylene)s. *Angew. Chem. Int. Ed. Engl.* **132**, 9165–9172 (2020).
41. Barron, L. & Buckingham, A. Rayleigh and Raman scattering from optically active molecules. *Mol. Phys.* **20**, 1111–1119 (1971).
42. Palomo, L. et al. Simultaneous detection of circularly polarized luminescence and Raman optical activity in an organic molecular lemniscate. *Angew. Chem. Int. Ed. Engl.* **61**, e202206976 (2022).
43. Moon, G. D. et al. Assembled monolayers of hydrophilic particles on water surfaces. *ACS Nano* **5**, 8600–8612 (2011).
44. Yang, H. et al. Visualization of chiral electronic structure and anomalous optical response in a material with chiral charge density waves. *Phys. Rev. Lett.* **129**, 156401 (2022).
45. Tutihasi, S. & Chen, I. Optical properties and band structure of trigonal selenium. *Phys. Rev.* **158**, 623–630 (1967).
46. Xie, J. et al. Defect-rich MoS₂ ultrathin nanosheets with additional active edge sites for enhanced electrocatalytic hydrogen evolution. *Adv. Mater.* **25**, 5807–5813 (2013).
47. Barragan-Yani, D. & Wirtz, L. Assessing the potential of perfect screw dislocations in SiC for solid-state quantum technologies. *Phys. Rev. Res.* **6**, L022055 (2024).
48. Zhu, J.-J. et al. Enhancing the sub-bandgap photo-response of silicon by inert element co-hyperdoping. *Opt. Lett.* **50**, 367–370 (2025).
49. Cheriton, R. et al. Two-photon photocurrent in InGaN/GaN nanowire intermediate band solar cells. *Commun. Mater.* **1**, 63 (2020).
50. Qin, J. et al. Controlled growth of a large-size 2D selenium nanosheet and its electronic and optoelectronic applications. *ACS Nano* **11**, 10222–10229 (2017).
51. Liu, P. et al. Photoconductivity of single-crystalline selenium nanotubes. *Nanotechnology* **18**, 205704 (2007).
52. Mort, J. Acoustoelectric current saturation in trigonal selenium. *Phys. Rev. Lett.* **18**, 540 (1967).
53. Yan, C., Singh, N., Cai, H., Gan, C. L. & Lee, P. S. Network-enhanced photoresponse time of Ge nanowire photodetectors. *ACS Appl. Mater. Interfaces* **2**, 1794–1797 (2010).
54. Zhang, B. Y. et al. Broadband high photoresponse from pure monolayer graphene photodetector. *Nat. Commun.* **4**, 1811 (2013).
55. Gupta, S. U. et al. Cryotronic low-powered strained polymorphic photodetector functionalized by palladium incorporated tin diselenide. *Adv. Opt. Mater.* **10**, 2201302 (2022).
56. Murray, C. B., Kagan, C. R. & Bawendi, M. G. Synthesis and characterization of monodisperse nanocrystals and close-packed nanocrystal assemblies. *Annu. Rev. Mater. Sci.* **30**, 545–610 (2000).
57. Colvin, V. L., Schlamp, M. C. & Alivisatos, A. P. Light-emitting diodes made from cadmium selenide nanocrystals and a semiconducting polymer. *Nature* **370**, 354–357 (1994).
58. Chen, Y.-Z. et al. Environmentally and mechanically stable selenium 1D/2D hybrid structures for broad-range photoresponse from ultraviolet to infrared wavelengths. *ACS Appl. Mater. Interfaces* **10**, 35477–35486 (2018).
59. Veeralingam, S., Borse, P. H. & Badhulika, S. High responsivity self-powered flexible broadband photodetector based on hybrid Selenium-PEDOT: PSS junction. *Org. Electron.* **108**, 106586 (2022).
60. Yu, X. et al. Self-powered photodetectors with high stability based on Se paper/P3HT: graphene heterojunction. *Nanomaterials* **14**, 1923 (2024).
61. Deng, W. et al. All-sprayed-processable, large-area, and flexible perovskite/MXene-based photodetector arrays for photo-communication. *Adv. Opt. Mater.* **7**, 1801521 (2019).
62. Qu, M., Tian, Y., Cheng, Y. B., Zhong, J. & Zhang, C. Whole-device mass-producible perovskite photodetector based on laser-induced graphene electrodes. *Adv. Opt. Mater.* **10**, 2201741 (2022).
63. Holmér, J. et al. Enhancing the NIR photocurrent in single GaAs nanowires with radial pin junctions by uniaxial strain. *Nano Lett.* **21**, 9038–9043 (2021).
64. Wang, M. et al. Silicon-based intermediate-band infrared photodetector realized by Te hyperdoping. *Adv. Opt. Mater.* **9**, 2001546 (2021).
65. Zhang, G. et al. High discrimination ratio, broadband circularly polarized light photodetector using dielectric achiral nanostructures. *Light Sci. Appl.* **13**, 275 (2024).
66. Guan, Q. et al. Pyro-phototronic effect induced circularly polarized light detection with a broadband response. *Adv. Sci.* **11**, 2404403 (2024).
67. Shi, W. et al. Fullerene desymmetrization as a means to achieve single-enantiomer electron acceptors with maximized chiroptical responsiveness. *Adv. Mater.* **33**, 2004115 (2021).
68. Zhao, Y. et al. Discovery of temperature-induced stability reversal in perovskites using high-throughput robotic learning. *Nat. Commun.* **12**, 2191 (2021).
69. Zhao, Y.-C. et al. Quantification of light-enhanced ionic transport in lead iodide perovskite thin films and its solar cell applications. *Light Sci. Appl.* **6**, e16243 (2017).
70. Nguyen, W. H., Bailie, C. D., Unger, E. L. & McGehee, M. D. Enhancing the hole-conductivity of spiro-OMeTAD without oxygen or lithium salts by using spiro (TFSI) 2 in perovskite and dye-sensitized solar cells. *J. Am. Chem. Soc.* **136**, 10996–11001 (2014).
71. Ismail, R. A., Mohammed, M. A., Abd-Alrahman, A. S. & Al-Rawi, I. I. Study the aging effect on the optoelectronic properties of HgI₂

- nanorods/Si heterojunction photodetector. *Opt. Quantum Electron.* **54**, 803 (2022).
72. Kim, B. J. et al. Improving the photoresponsivity and reducing the persistent photocurrent effect of visible-light ZnO/quantum-dot phototransistors via a TiO₂ layer. *J. Mater. Chem. C* **8**, 16384–16391 (2020).

Acknowledgements

J.Y. and J.K. acknowledge support from the Korea government (the Ministry of Science and ICT, the Ministry of Trade, Industry and Energy, the Ministry of Health & Welfare, the Ministry of Food and Drug Safety) (Project Number: 9991006823, KMDF_PR_20200901_0150); Basic Science Research Program through the National Research Foundation of Korea (NRF) funded by the Ministry of Education (grant nos. NRF-2021R1C1C1009766, RS-2024-00357142); the Samsung Electronics Co., Ltd. (IO201209-07914-01); KAIST Center for Contemplative Science Internal Research Project (grant no. N11250001); the Pukyong National University Industry-university Cooperation Foundation's 2024 (202408220001). The authors are grateful to Sang-Gil Lee at the Daejeon Center of the Korea Basic Science Institute for technical assistance of the crystal analysis with Libra 200 MC TEM. This work was performed under the auspices of the U.S. Department of Energy by Lawrence Livermore National Laboratory (LLNL) under Contract DE-AC52-07NA27344. W.J.C. gratefully acknowledges the LLNL Laboratory Directed Research and Development (LDRD) Program for funding support of this project under No.22-ERD-056 and 24-LW-035.

Author contributions

Under the supervision of J.Y., J.K. designed the experiments and conducted the research. J.B.J. and M.G.L. fabricated the electrode and measured the photocurrent of the device under the supervision of K.M.K. S.J. performed the 2D ROA analysis. W.J.C. performed Mueller polarimetry measurements. All authors discussed the results and commented on the manuscript.

Competing interests

The authors declare no competing interests.

Additional information

Supplementary information The online version contains supplementary material available at <https://doi.org/10.1038/s41467-025-59091-9>.

Correspondence and requests for materials should be addressed to Jihyeon Yeom.

Peer review information *Nature Communications* thanks Zhenzhou Cheng, Longzhen Qiu, and the other anonymous reviewers for their contribution to the peer review of this work. A peer review file is available.

Reprints and permissions information is available at <http://www.nature.com/reprints>

Publisher's note Springer Nature remains neutral with regard to jurisdictional claims in published maps and institutional affiliations.

Open Access This article is licensed under a Creative Commons Attribution-NonCommercial-NoDerivatives 4.0 International License, which permits any non-commercial use, sharing, distribution and reproduction in any medium or format, as long as you give appropriate credit to the original author(s) and the source, provide a link to the Creative Commons licence, and indicate if you modified the licensed material. You do not have permission under this licence to share adapted material derived from this article or parts of it. The images or other third party material in this article are included in the article's Creative Commons licence, unless indicated otherwise in a credit line to the material. If material is not included in the article's Creative Commons licence and your intended use is not permitted by statutory regulation or exceeds the permitted use, you will need to obtain permission directly from the copyright holder. To view a copy of this licence, visit <http://creativecommons.org/licenses/by-nc-nd/4.0/>.

© The Author(s) 2025